Check for updates

OPEN

Predicting the influence of particle size on the glass transition temperature and viscosity of secondary organic material

Markus Petters✉ & Sabin Kasparoglu

Atmospheric aerosols can assume liquid, amorphous semi-solid or glassy, and crystalline phase states. Particle phase state plays a critical role in understanding and predicting aerosol impacts on human health, visibility, cloud formation, and climate. Melting point depression increases with decreasing particle diameter and is predicted by the Gibbs–Thompson relationship. This work reviews existing data on the melting point depression to constrain a simple parameterization of the process. The parameter ξ describes the degree to which particle size lowers the melting point and is found to vary between 300 and 1800 K nm for a wide range of particle compositions. The parameterization is used together with existing frameworks for modeling the temperature and RH dependence of viscosity to predict the influence of particle size on the glass transition temperature and viscosity of secondary organic aerosol formed from the oxidation of α-pinene. Literature data are broadly consistent with the predictions. The model predicts a sharp decrease in viscosity for particles less than 100 nm in diameter. It is computationally efficient and suitable for inclusion in models to evaluate the potential influence of the phase change on atmospheric processes. New experimental data of the size-dependence of particle viscosity for atmospheric aerosol mimics are needed to thoroughly validate the predictions.

Atmospheric aerosols play a central role in atmospheric chemistry by providing surface and volume for multiphase reactions to proceed. Crystalline solid or amorphous viscous particles contain little or no water. At moderate relative humidity (RH) some particles form concentrated aqueous solutions, and at high RH ($> 80\%$) particle-bound water may become the dominant aerosol component[1]. Diffusion of gases through solids and intraparticle mixing times in solids are slow. Thus, chemical reactions within the bulk of a solid particle may be slow (or effectively impossible)[2–5]. Similarly, absorptive gas-particle partitioning is predicated on the existence of a well-mixed liquid organic phase. When the organic phase is viscous, gas-particle equilibration time scales of semi-volatile organic compounds can become long ($>> 1$ h), thus necessitating kinetic instead of thermodynamic frameworks to model secondary organic aerosol formation[6–9]. Measured equilibration time scales for water in viscous and glassy solids are fast at warmer temperatures ($T > -10\,°C$)[10–13]. In turn, viscosity exerts little influence on atmospheric processes involving water uptake. However, at upper-free tropospheric temperatures ($T < -40\,°C$), water uptake is slow[14]. This leaves solid surfaces partially or fully intact for considerable duration at humidities exceeding ice saturation. Some of these surfaces may serve as heterogeneous ice nucleation sites[11,15–17] and thus may influence ice crystal concentration in cirrus clouds. The above mentioned effects imply that particle phase state plays a critical role in understanding and predicting aerosol impacts on human health, visibility, cloud formation, and climate[18].

Particle viscosity can be used to categorize the amorphous particle phase state into liquid (10^{-3} Pa s, "water" to 10^4 Pa s, "peanut butter"), semi-solid (10^4–10^{12} Pa s, "glass"), and glassy solid ($> 10^{12}$ Pa s) regimes. Particle viscosity sharply increases with decreasing temperature[19,20]. A common convention is to equate the temperature at which the viscosity reaches 10^{12} Pa s with the glass transition temperature that is obtained using differential scanning calorimetery[21]. Zobrist et al.[22] first suggested that organic particles might form glassy states at low RH and cold temperatures. Soon after, Virtanen et al.[23] showed that secondary organic aerosol (SOA) generated in plant-chambers and atmospheric organic aerosol (OA) can exist in solid states. This was inferred from "bounce

Department of Marine, Earth, and Atmospheric Sciences, NC State University, Raleigh 27695-8208, USA. ✉email: mdpetter@ncsu.edu

factor" measurements, where the bounce factor refers to the fraction of particles that rebound upon impaction on a surface. Particles that deform upon impaction are more likely to adhere to the surface than solid particles; larger bounce factors thus indicate a more solid phase state.

The initial discovery that ambient OA particles bounce implies that they are semi-solid at room temperature. A large number of follow-up studies investigated viscosity of ambient organic aerosol and environmental chamber aerosol. These studies were recently reviewed by Reid et al.[18]. The main thrusts described therein are briefly summarized here. A number of new techniques were developed to better quantify aerosol phase state[24–30]. Factors that increase OA viscosity have been identified to be increasing compound molecular weight[31], O:C ratio[32], and functional group composition[19,33]. Viscosity and volatility are inversely correlated[19,34,35]. Under dry conditions and at room temperature many secondary organic aerosols are semi-solid. The extent of the reduction in viscosity with RH depends on the hygroscopicity of the aerosol[29,36–38]. Monoterpenes and aromatic precursors produce more viscous particles than isoprene SOA[27,30,37,39,40]. Ambient SOA phase state follows a diurnal cycle, with higher viscosity observed during nightime[41]. Reactive uptake has been shown to create viscous shells or cores[42,43]. Under humid conditions water uptake rapidly reduces viscosity. Measurements and models quantifying the amorphous phase state diagram over a wide range of temperature and humidity have been developed[16,22,31,40,44–46]. The relationships between viscosity and diffusion-coefficients, to first order predicted by the Stokes–Einstein equation, have been clarified. The Stokes–Einstein equation holds for predicting the diffusion of larger organic molecules, but errs for small molecules such as water[2,9–11,13,47,48]. First estimates of the prevalence of gassy organic states in the atmosphere have been made[19,32,49]. The potential dependence of viscosity on particle size has received less attention.

As particle size decreases, the surface to volume ratio increases and a number of aerosol physicochemical properties are affected. Due to surface tension, the vapor pressure over a curved particle increases (Kelvin effect) and melting point decreases (Gibbs–Thompson effect). Surface tension itself increases with decreasing particle diameter below the Tolman length[50,51]. Furthermore with decreasing particle diameter, the deliquescence relative humidity and efflorescence relative humidity increases[52–54], the equilibrium hygroscopic growth factor decreases[55], the condensation coefficient of the gas molecule to the particle surface decreases[56], and liquid–liquid phase separation is suppressed[57–60]. Virtanen et al.[23,61] showed that the bounce factor of organic particles produced by OH dominated oxidation of pine emitted volatile organic compounds sharply decreases for particles with $D < 30$ nm, but not for solid ammonium sulfate particles. This implies either that composition for $D < 30$ nm SOA differs from those of the larger particles, or that size influences particle viscosity. Cheng et al.[62] propose that a critical diameter exists at which solid particles liquefy and that the inverse of the critical diameter linearly increases with the temperature of the bulk phase transition.

The above body of literature does not include a clear methodology to predict the influence of particle size on the melting point, the glass transition temperature, and the temperature and humidity dependence of particle viscosity. Such predictions are needed to model the phase state of atmospheric particulate matter. This work presents a computationally inexpensive framework that is suitable for treating the size dependence of particle phase state. Available literature data are reviewed to constrain the model. Predictions are made for SOA generated from α-pinene. Parameters that are important to the prediction of size dependent phase state are identified. Critical needs for future measurements characterizing the size dependence of phase transitions are described.

Model

Melting-point depression. The melting point depression for a spherical particle is computed using the Gibbs–Thompson relationship[63]

$$\Delta T = \frac{6\sigma_{l/s} v_{s,m}}{D \Delta_m S} \qquad (1)$$

where T is the temperature, $\Delta T = (T_{bulk} - T)$ is the melting point depression defined as the difference between the melting point temperature of the bulk material and actual melting temperature, D is the particle diameter, $\sigma_{l/s}$ is the liquid/solid interfacial tension, $v_{s,m}$ is the molar volume of solid, $\Delta_m S$ is the molar entropy of the phase change at the melting temperature. The scaling of the influence of curvature, given by the prefactor 6 in Eq. 1, differs between different authors[63]. Equation 1 can be parameterized as

$$\Delta T = \xi D^{-1} \qquad (2)$$

where $\xi = 6\sigma_{s/l} v_{s,m}/\Delta_m S$ is a parameter that subsumes the prefactor, the unknown physicochemical properties and depends on the particle composition.

Figure 1 summarizes available literature data of melting point depression for various composition categories. The data are obtained from a range of experimental techniques and include some molecular dynamic simulations. The data are approximately consistent with the Gibbs–Thompson slope of -1 in log–log space for the majority of the data, with obvious deviations for lead, tin, and aqueous NaCl. The deviations from Gibbs–Thompson for led and tin below 10 nm have been noted before[64,65]. Reasons for the deviation from Gibbs–Thompson include variation of surface tension and entropy of melting with size, as well as particle shape effects[65]. There is significant variability between different compounds. For example, a melting point depression of 30 K is required to liquify 10 nm polyethylene while 200 K is required for aqueous ammonium sulfate, lead or gold particles. There is no obvious clustering of broad compound classes, i.e. metals, inorganic salts, and organics. Nonetheless, the Gibbs–Thompson slope of -1 in log–log space is a reasonable approximation and there appears to be a limited range of ξ values, despite a large variability of bulk melting point temperature (414–1337 K) for the graphed compounds. For the data shown, ξ varies between 300 and 1800 K nm.
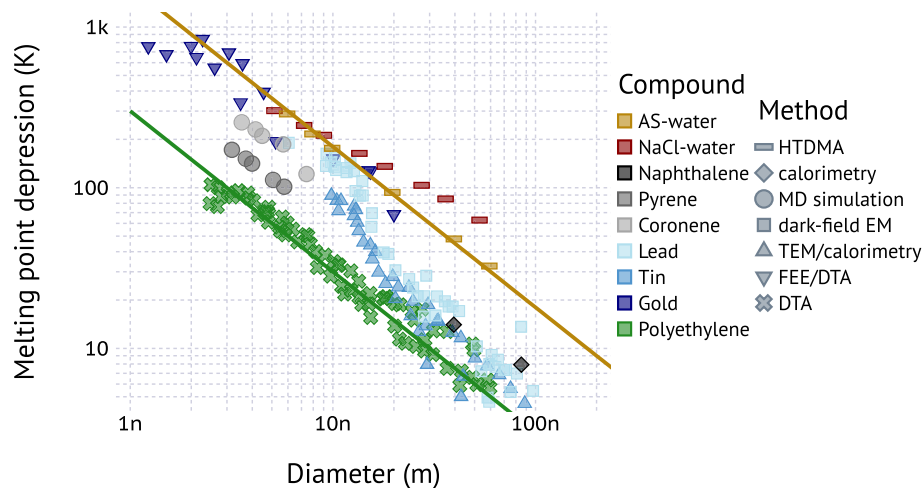
Figure 1. Summary of literature data for the size melting point depression versus size. Colors indicate the chemical composition groups: aqueous salt solutions (red/gold), polycyclic aromatic hydrocarbons (black/gray), metal particles (blue), polyethylene (green). Shapes denote the method used to generate the data. *HTDMA* humidified tandem differential mobility analyzer[52,55], *MD* molecular dynamics simulation[66], *(T)EM* (transmission) electron microscopy[67,68], *FEE* field-electron emission[69], *DTA* differential thermal analysis[70]. Solid lines correspond to Eq. 2 with $\xi = 1800$ K nm (salmon) and $\xi = 300$ K nm (green). Data sources are listed in the methods section.

Glass-transition and temperature-dependence of viscosity. The glass transition temperature is related to the bulk melting temperature via $T_g = gT_m$, which is known as the Boyer–Kauzmann rule. The value of g is 0.7 ± 0.2 (supplemental information). It follows that the size dependence of the glass transition temperature is

$$T_g = T_g^{bulk} - g\xi D^{-1} \tag{3}$$

where T_g^{bulk} is the glass transition temperature for the bulk material. To the authors' knowledge, no data on the melting point depression of amorphous glassy material is available. Equation 3 is therefore an untested hypothesis that will need to be validated against experimental data in future studies.

At temperatures warmer than T_g, but colder than T_m, viscosity decreases over many orders of magnitude. Angell[71,72] showed that viscosity scaled by T_g can be modeled using a simple parameterization

$$\log_{10} \eta = -5 + 0.434\left(\frac{39.17 D_A}{D_A T/T_g + 39.17 T/T_g - 39.17}\right) \tag{4}$$

where η is the viscosity and D_A is the fragility parameter. Figure 2 illustrates the Angell representation of viscosity. At $T_g/T = 1$ the particle is a glass and viscosity is taken to be 10^{12} Pa s. At $T > T_g$, viscosity decreases. At very high temperature the viscosity approaches that of a gas, $\sim 10^{-5}$ Pa s. The Arrhenius representation of the temperature dependence of viscosity corresponds to linear relationship in log-linear coordinates. Compounds following the Arrhenius law are dubbed "strong" glasses[71]. Fragile glasses deviate from the Arrhenius law and are described by Eq. 4. Shiraiwa et al.[32] estimate $5 < D_A < 20$ for typical compounds found in SOA. Only very limited data on the temperature dependence of viscosity for SOA are available[40]. The glass-transition temperature in that work is from an extrapolation of temperature-dependent viscosity data. Extrapolated T_g from that method agrees within $\sim \pm 10$ K of T_g obtained from scanning calorimetry for citric acid and sucrose[44,45]. The fragility parameter for α-pinene SOA is consistent with $D_A = 7$. Importantly, aqueous solutions of sucrose may be described using a single fragility parameter[73]. This provides some justification to apply $D_A = 7$ to dry SOA and aqueous solutions of SOA that form due to hygroscopic growth at elevated relative humidity.

Humidity-dependence. Humidity dependence is modeled as described in Rothfuss and Petters[44]. T_g of the binary solute and water system is generally is estimated using the Gordon–Taylor[74] mixing rule[16,22,31,32,44,45,75–77].

$$T_g = \frac{[1 - w_s(RH)]T_{g,w} + \frac{1}{k_{GT}} w_s(RH) T_{g,s}}{1 - w_s(RH) + \frac{1}{k_{GT}} w_s(RH)} \tag{5}$$

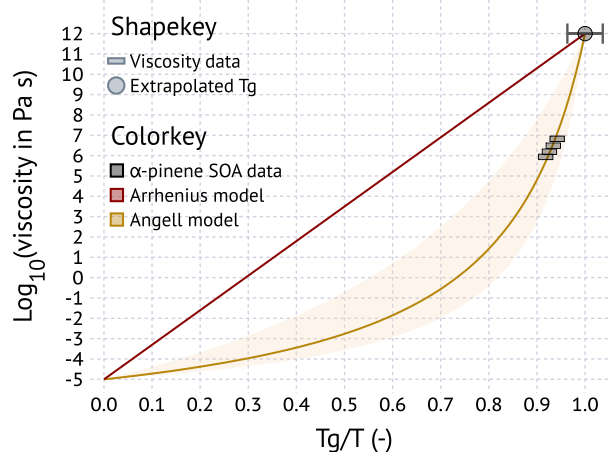$$w_s = \left(1.0 + \kappa_m \frac{a_w}{1 - a_w}\right)^{-1} \tag{6}$$

Figure 2. Angell[71] representation of viscosity scaled by T_g. Viscosity and T_g data are from Petters et al.[40]. The error bar on T_g correspond to ± 10 K uncertainty. The solid golden line and shaded area correspond to $D_A = 7$ and $5 < D_A < 20$, respectively.

where w_s is the weight fraction of solute, a_w is the water activity ($a_w = 0.01RH\exp(A/D)^{-1}$, $A = 8.69251 \times 10^{-6}\sigma_{s/a}/T^{78}$, $\sigma_{s/a}$ is the surface tension, RH is the relative humidity in %), κ_m is the mass based hygroscopity parameter[79], T_g is the glass transition temperature of the mixture, $T_{g,w}$ the glass transition temperature of water, $T_{g,s}$ is the glass transition temperature of the solute and k_{GT} is the Gordon–Taylor constant. In contrast to the formulation described in Rothfuss and Petters[44], Eq. 6 accounts for the effect of curvature on water content.

The Gordon–Taylor mixing rule has its origin in polymer science and for some polymer systems the Gordon–Taylor constant can obtained from the density and expansion coefficient. This however fails when applying the rule to non-polymers and systems containing water. In such systems k_{GT} becomes an empirical coefficient associated with the compound. A number of expressions having similar mathematical form have been proposed[80]. Variations of the mixing rule include the Fox[81] equation, the Couchman and Karasz[82] equation, which is as the Gordon–Taylor rule but using mole fraction as composition variable and heat capacity ratios to express k, and the Kwei[83] equation, which is as the Gordon–Taylor rule but also includes higher order terms. Secondary organic aerosol is a mixture comprising 100 s of components[84,85]. One approach is to group the organic compounds together and then use a binary Gordon–Taylor mixing rule to treat mixtures of water and the lumped organic fraction[86], which is denoted as the quasi-binary assumption.

Here the Gordon–Taylor mixing rule is applied to SOA using the quasi-binary assumption with the following inputs. The glass transition temperature for α-pinene-derived SOA is $T_{g,s}^{bulk} = 271.7 \pm 10$ K[40]. The ± 10 K estimate denotes the accuracy of a single measurement and does not account for composition differences that arise from differences in SOA generation method between studies. Furthermore, $T_{g,w} = 136$K[31], $k_{GT} = 2.5 \pm 1.5$[22,31,87] and $\kappa_m = 0.04 \pm 0.035$. The range $\kappa_m = 0.04 \pm 0.035$ neglects the potential systematic variation of κ_m with relative humidity. Further details are provided in the methods and supplemental information.

Viscosity model. Let the generic function definitions $T_g^{size}(T_g^{bulk}, D)$ denote Eq. 3, $T_g^{bulk}(w_s(RH), T_{g,s}^{bulk})$ denote Eq. 5, $w_s(RH)$ denote Eq. 6, and $\eta_A(T, T_g)$ denote Eq. 4. Viscosity as a function of T, RH, and D is computed via function composition.

$$\eta(T, RH, D) = \eta_A\left(T, T_g^{size}(T_g^{bulk}(w_s(RH), T_{g,s}^{bulk}), D)\right) \tag{7}$$

where the composite function $\eta(T, RH, D)$ also depends on the solute parameters $T_{g,s}^{bulk} = 271.7 \pm 10K$, $\kappa_m = 0.04 \pm 0.035$, $k_{GT} = 2.5 \pm 1.5$, $D_A = 7$, $g = 0.7$ and $\xi = 1050 \pm 750$ K nm; the values are estimates for α-pinene SOA, except for the range in ξ, which is based on the data in Fig. 1. In the limit of infinitely large particles, this model is identical to the model of DeRieux et al.[87]. However, the solute parameters differ from DeRieux et al.[87] due to newly available experimental constraints on fragility and different assumptions made about hygroscopicity. A detailed representation of Eq. 7 is given in the supplemental information.

Results and discussion

Figure 3 shows measured and predicted viscosity of α-pinene SOA at room temperature as a function of relative humidity without taking the potential size dependence of T_g into account. The slope of the η-RH relationship is determined by k_{GT} and κ_m. Data from Pajunaja et al.[90] and Renbaum-Wolff et al.[30] show viscosity > 10^9 Pa s at RH < 30% and fall outside the shaded area. Increasing the range in $T_{g,s}^{bulk}$ to ± 25 K, as was assumed in DeRieux et al.[87], would include those points inside the shaded area. $T_{g,s}$ depends on molecular weight and functional group composition and it small differences in these parameters have a large effect on $T_{g,s}$. Thus composition differences between the studies likely explain the higher viscosity in these experiments[40]. Overall the model
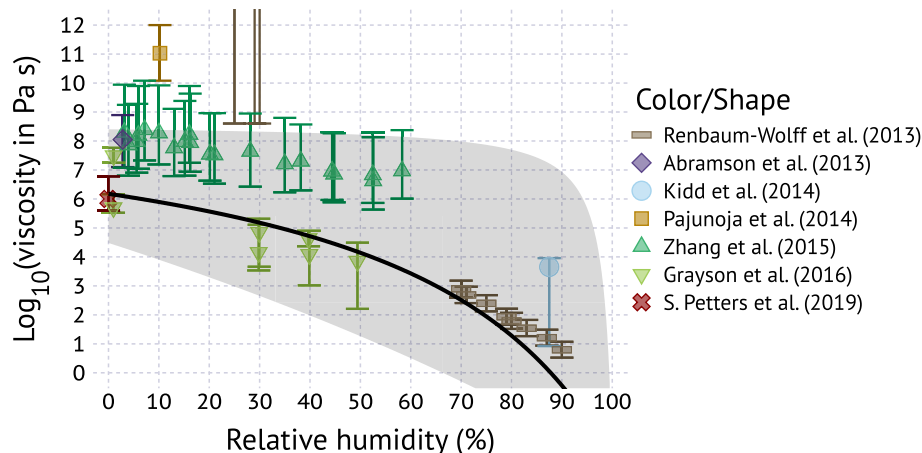
Figure 3. Measured[27,30,40,88–91] and predicted viscosity of α-pinene SOA at room temperature as a function of relative humidity. The measurements by Renbaum-Wolff et al.[30] at RH 20-30% correspond to a lower limit estimate of their poke-flow measurements (horizontal bar) with possible values being up to, or exceeding 10^{12} Pa s. The solid line and gray shaded area corresponds to $T_{g,s}^{bulk} = 271.7 \pm 10$ K, $\kappa_m = 0.04 \pm 0.035$, $k_{GT} = 2.5 \pm 1.5$, $g = 0.7$, and $D_A = 7$.
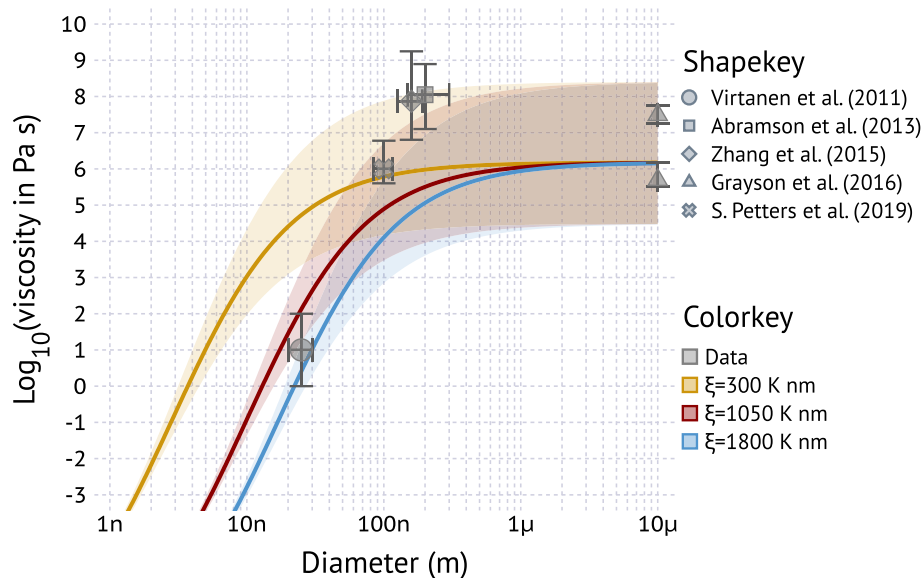

Figure 4. Measured and predicted viscosity of α-pinene SOA at room temperature as a function of particle diameter. The solid lines and shaded area corresponds to predicted viscosity assuming $T_{g,s}^{bulk} = 271.7 \pm 10$ K, $\kappa_m = 0.04 \pm 0.035$, $k_{GT} = 2.5 \pm 1.5$, $D_A = 7$, $g = 0.7$, and RH = 0%. Colors delineate different values of ξ spanning the range of values shown in Fig. 1.

and parameter ranges are in reasonable agreement with most of the published data. The remainder of this work will use the parameter ranges $T_{g,s}^{bulk} = 271.7 \pm 10$ K, $\kappa_m = 0.04 \pm 0.035$, $k_{GT} = 2.5 \pm 1.5$, $D_A = 7$, $g = 0.7$ and $\xi = 1050 \pm 750$ K nm to explore the dependence of viscosity on particle size.

Figure 4 shows the measured and predicted viscosity of α-pinene SOA at room temperature as a function of particle diameter. Data are as the same as in Fig. 3 for the lowest RH reported but plotted at the measurement diameter. The Grayson et al.[91] are obtained using a "bulk" poke-flow method and are plotted at 10 μm diameter for reference. Note that the Virtanen et al.[61] data differ in several respects. The data are taken at RH = 31%, significantly higher than the other values (0–2%). The SOA is from oxidation of pine emitted VOCs and not pure α-pinene and the data are not direct measurements of viscosity. Virtanen et al. observed a decrease in rebound fraction in an impactor for $D < 30$ nm. Upon impaction, a fraction of the energy is dissipated due to particle deformation (i.e. viscosity) while the remainder is available for rebound. Rebound occurs when the kinetic energy exceeds the energy adhesion[61]. Virtanen et al. show that the predominant impaction energy of the smaller particles is larger than the impaction energy of the larger particles, and thus that the decreasing rebound

fraction indicates a decrease in viscosity[36,92]. Assigning a viscosity to the Virtanen data in retrospect is difficult. Bateman et al.[36] calibrated a different impactor at a different size with sucrose and report that the viscosity range for that transition is 1–100 Pa s. That value range is expected to depend on the impactor surface properties and flow dynamics. Slade et al.[41] used a low pressure impactor similar in design to that in Virtanen et al. and classify particles with a rebound fraction < 0.2 as "liquid" while assigning "liquid" a viscosity < 100 Pa s. Therefore, the Virtanen et al.[61] observations, which show bounce fraction < 0.2 at ∼ 25 nm, are graphed in Fig. 4 having viscosity 1–100 Pa s. Future measurements are needed to confirm that value.

As expected, the predicted dependence of viscosity on particle size depends on ξ, with larger values of ξ corresponding to a larger decrease in viscosity with decreasing size. The data are broadly consistent with $1050 < \xi < 1800$ K nm. The exact value remains unclear due to the need to juxtapose data from different sources. This results in an the imperfect match of relative humidity. There are also differences in chemical composition due to differences in mass loading, oxidant exposure, size-dependence of composition, aerosol preparation method and aerosol age, all of which may affect the glass transition temperature and viscosity. Finally, only a single data point at $D < 100$ nm is available. This point is also taken at elevated relative humidity. If humidity influences the observed viscosity, the viscosity under dry conditions would have been higher, which in turn would alias as $\xi < 1050$. Due to the very limited available aerosol viscosity data a preliminary range $300 < \xi < 1800$ K nm for organic aerosol is proposed, which is based on the survey presented in Fig. 1. Systematic studies of the effect of particle size on viscosity are needed, including the study of pure compounds and of complex mixtures such as SOA.

The model predictions show a decrease in viscosity to that of a thin liquid, defined as $< 10^{-3}$ Pa s at 1.6, 5.5, and 9.3 nm for $\xi = 300, 1050$, and 1800 K nm, respectively. Changing relative humidity or temperature in the model changes the viscosity at large size, but it has a negligible effect on the slope of viscosity vs. size at small diameter and the size of the intersection with 10^{-3} Pa s. The uncertainty in the g value from application of the Boyer–Kauzmann rule ($g = 0.7 \pm 0.2$) slightly alters the intersection with 10^{-3} Pa s. Sensitivity analysis to these parameters is provided in the supplemental information. The predicted decreased below 10^{-3} Pa s implies that the mixture is behaving more like a gas and is equivalent to volatilization due to decreasing particle curvature and increasing Kelvin effect.

The model formulated in Eq. 7 only relies on simple algebraic functions. It is computationally efficient and thus suitable for inclusion in atmospheric models. Input parameters such as $T_{g/s}$ and κ_m can be predicted from various proxies for organic aerosol composition[32,87,93–95]. However, prediction of the fragility parameter (D_A), Gordon–Taylor constant (k_{GT}) and ξ from composition data are not yet available. Nevertheless, reasonably constrained ranges for these parameters exist and have been identified here or in previous studies. The parameter $\xi = 6\sigma_{s/l}v_{s,m}/\Delta_m S$ can be predicted from first principles provided $\sigma_{s/l}$, $v_{s,m}$, and $\Delta_m S$ data are available. For example, crystalline pyrene has $\sigma_{s/l} = 22.8 \times 10^{-3}$ J m^{-2} (ref.[96]), $v_{s,m} = 1.59 \times 10^{-4}$ m^3 mol^{-1} (based on molecular weight and density), and $\Delta_m S = 40.97$ J mol^{-1} K^{-1} (ref.[97]). Therefore $\xi = 6\sigma_{s/l}v_{s,m}/\Delta_m S = 531$ K nm is predicted. A fit to the pyrene data from MD simulations in Fig. 1 yields 560 K nm. Systematic molecular dynamics simulations[66,98] systematic evaluation of available surface tension and entropy of melting data may provide additional constraints on ξ and its dependence on composition.

Conclusions

Data of the melting point depression as a function of particle size have been reviewed. A parameter ξ is abstracted from the Gibbs–Thompson relationship, where ξ characterizes the size dependence of the melting point for a fixed particle composition. The parameterization is applied to predict changes in glass transition temperature and viscosity as a function of size. Only limited aerosol data are available to validate the model. From these data a preliminary range $300 < \xi < 1800$ K nm for organic aerosol is proposed. New experimental data of the size-dependence of particle viscosity for atmospheric aerosol mimics are needed to thoroughly validate the predictions made herein. The model framework, together with the identified parameter ranges, can be used to evaluate the potential influence of melting point depression on atmospheric processes.

Methods

Melting-point depression. Melting point depression data collated in Fig. 1 were digitized from data displayed in figures in the literature. Details about the digitization method are given in the supplemental information. The digitized data plotted are summarized in a comma delineated text file that contains the melting point depression (ΔT), particle diameter (D), the source citation, the source figure that was digitized, and the method that was used to generate the data. Tin data are taken from Fig. 2 in Koppes et al.[99] including data from Wronski[68] and Lai et al.[100]. Gold data correspond to spherical gold particles summarized in Fig. 2 by Lu et al.[101] with data from Castro et al.[69] and Dick et al.[102]. Lead data are taken from Fig. 2 in David et al.[67]. Pyrene and coronene data are taken from Fig. 5 in Chen et al.[98]; naphthalene data are taken from Fig. 4 in Jackson and McKenna[103]. Polyethylene data is from Fig. 1 in Jiang et al.[66] including data for linear alkanes[104], cyclic alkanes[105], and chain-extended polyethylene[70]. Data for aqueous salt solutions is taken from Fig. 5 in Cheng et al.[62] with data derived from Biskos et al.[52,55].

Hygroscopicity data. Volume-based hygroscopicity parameter[106] data for α-pinene SOA were digitized from data displayed in figures and tables in the literature[38,107,108]. The digitized data plotted are summarized in a comma delineated text file that contains relative humidity, κ_v value, and the source citation. Volume-based hygroscopicity parameter[106] data are converted to mass-based hygroscopicity[79] using

$$\kappa_m = \kappa_v \frac{\rho_w}{\rho_s} \tag{8}$$

where κ_m is the mass-based hygroscopicity parameter[79], ρ_w and ρ_s are the density of water and solute, respectively. The density of α-pinene SOA in these studies is unknown. Kuwata et al.[109] report $1.23 < \rho_s < 1.46 \,\mathrm{g\,cm^{-3}}$ for α-pinene SOA. The uncertainty due to unknown density in the conversion from κ_v to κ_m is unimportant relative to the reported range in values. The data are graphed in the supplemental information.

Viscosity data. Viscosity data collated in Figs. 2, 3 and 4 were digitized from data displayed in figures and tables in the literature[27,30,40,88–91]. The digitized data plotted are summarized in comma delineated text files. Viscosity data points in Fig. 2 were generated as follows. The logistic fit to the particle shape parameter measurement for α-pinene (supplemental information ref.[40]) was solved for the interval $[x_0 - \sigma, x_0 + \sigma]$, where x_0 corresponds to the mean and σ to the slope of the transition, and $x_0 = 20.2\,^\circ\mathrm{C}$ and $\sigma = 4.93$ for α-pinene. The interval was discretized into $2.5\,^\circ\mathrm{C}$ steps. The interval only determines the density of points plotted in Fig. 2. The shape parameter was converted to viscosity using sintering theory[25,110] and the temperature was normalized by the T_g extrapolated from the same measurements.

Data availability

All data and scripts used to create the figures in this manuscript are freely available through GitHub and DockerHub. Data and scriptsare archived in an online data repository at https://doi.org/10.5281/zenodo.3824214.). Further details are in the supplemental information.

References

1. Nguyen, T. K. V. *et al.* Trends in particle-phase liquid water during the Southern Oxidant and Aerosol Study. *Atmos. Chem. Phys.* **14**, 10911–10930. https://doi.org/10.5194/acp-14-10911-2014 (2014).
2. Shiraiwa, M., Ammann, M., Koop, T. & Pöschl, U. Gas uptake and chemical aging of semisolid organic aerosol particles. *Proc. Natl. Acad. Sci.* **108**, 11003–11008. https://doi.org/10.1073/pnas.1103045108 (2011).
3. Slade, J. H. & Knopf, D. A. Multiphase OH oxidation kinetics of organic aerosol: the role of particle phase state and relative humidity. *Geophys. Res. Lett.* **41**, 5297–5306. https://doi.org/10.1002/2014GL060582 (2014).
4. Gržinić, G., Bartels-Rausch, T., Berkemeier, T., Türler, A. & Ammann, M. Viscosity controls humidity dependence of N_2O_5 uptake to citric acid aerosol. *Atmos. Chem. Phys.* **15**, 13615–13625. https://doi.org/10.5194/acp-15-13615-2015 (2015).
5. Shrivastava, M. *et al.* Global long-range transport and lung cancer risk from polycyclic aromatic hydrocarbons shielded by coatings of organic aerosol. *Proc. Natl. Acad. Sci.* **114**, 1246–1251. https://doi.org/10.1073/pnas.1618475114 (2017).
6. Vaden, T. D., Imre, D., Beránek, J., Shrivastava, M. & Zelenyuk, A. Evaporation kinetics and phase of laboratory and ambient secondary organic aerosol. *Proc. Natl. Acad. Sci.* **108**, 2190–2195. https://doi.org/10.1073/pnas.1013391108 (2011).
7. Zaveri, R. A. *et al.* Growth kinetics and size distribution dynamics of viscous secondary organic aerosol. *Environ. Sci. Technol.* **52**, 1191–1199. https://doi.org/10.1021/acs.est.7b04623 (2018).
8. Ye, Q. *et al.* Following particle–particle mixing in atmospheric secondary organic aerosols by using isotopically labeled terpenes. *Chem* **4**, 318–333. https://doi.org/10.1016/j.chempr.2017.12.008 (2018).
9. Li, Y. & Shiraiwa, M. Timescales of secondary organic aerosols to reach equilibrium at various temperatures and relative humidities. *Atmos. Chem. Phys.* **19**, 5959–5971. https://doi.org/10.5194/acp-19-5959-2019 (2019).
10. Price, H. C. *et al.* Quantifying water diffusion in high-viscosity and glassy aqueous solutions using a Raman isotope tracer method. *Atmos. Chem. Phys.* **14**, 3817–3830. https://doi.org/10.5194/acp-14-3817-2014 (2014).
11. Lienhard, D. M. *et al.* Viscous organic aerosol particles in the upper troposphere: diffusivity-controlled water uptake and ice nucleation?. *Atmos. Chem. Phys.* **15**, 13599–13613. https://doi.org/10.5194/acp-15-13599-2015 (2015).
12. Rothfuss, N. E., Marsh, A., Rovelli, G., Petters, M. D. & Reid, J. P. Condensation kinetics of water on amorphous aerosol particles. *J. Phys. Chem. Lett.* **9**, 3708–3713. https://doi.org/10.1021/acs.jpclett.8b01365 (2018).
13. Tandon, A., Rothfuss, N. E. & Petters, M. D. The effect of hydrophobic glassy organic material on the cloud condensation nuclei activity of particles with different morphologies. *Atmos. Chem. Phys.* **19**, 3325–3339. https://doi.org/10.5194/acp-19-3325-2019 (2019).
14. Zobrist, B. *et al.* Ultra-slow water diffusion in aqueous sucrose glasses. *Phys. Chem. Chem. Phys.* **13**, 3514–3526. https://doi.org/10.1039/C0CP01273D (2011).
15. Murray, B. J. *et al.* Heterogeneous nucleation of ice particles on glassy aerosols under cirrus conditions. *Nat. Geosci.* **3**, 233 (2010).
16. Berkemeier, T., Shiraiwa, M., Pöschl, U. & Koop, T. Competition between water uptake and ice nucleation by glassy organic aerosol particles. *Atmos. Chem. Phys.* **14**, 12513–12531. https://doi.org/10.5194/acp-14-12513-2014 (2014).
17. Ignatius, K. *et al.* Heterogeneous ice nucleation of viscous secondary organic aerosol produced from ozonolysis of α-pinene. *Atmos. Chem. Phys.* **16**, 6495–6509. https://doi.org/10.5194/acp-16-6495-2016 (2016).
18. Reid, J. P. *et al.* The viscosity of atmospherically relevant organic particles. *Nat. Commun.* **9**, 956. https://doi.org/10.1038/s41467-018-03027-z (2018).
19. Rothfuss, N. E. & Petters, M. D. Influence of functional groups on the viscosity of organic aerosol. *Environ. Sci. Technol.* **51**, 271–279. https://doi.org/10.1021/acs.est.6b04478 (2017).
20. Fulcher, G. S. Analysis of recent measurements of the viscosity of glasses. *J. Am. Ceram. Soc.* **8**, 339–355. https://doi.org/10.1111/j.1151-2916.1925.tb16731.x (1925).
21. Debenedetti, P. G. & Stillinger, F. H. Supercooled liquids and the glass transition. *Nature* **410**, 259–267. https://doi.org/10.1038/35065704 (2001).
22. Zobrist, B., Marcolli, C., Pedernera, D. A. & Koop, T. Do atmospheric aerosols form glasses?. *Atmos. Chem. Phys.* **8**, 5221–5244. https://doi.org/10.5194/acp-8-5221-2008 (2008).
23. Virtanen, A. *et al.* An amorphous solid state of biogenic secondary organic aerosol particles. *Nature* **467**, 824 (2010).
24. Rothfuss, N. E., Petters, S. S., Champion, W. M., Grieshop, A. P. & Petters, M. D. Characterization of a dimer preparation method for nanoscale organic aerosol. *Aerosol Sci. Technol.* **39**, 998–1011. https://doi.org/10.1080/02786826.2019.1623379 (2019).
25. Rothfuss, N. E. & Petters, M. D. Coalescence-based assessment of aerosol phase state using dimers prepared through a dual-differential mobility analyzer technique. *Aerosol Sci. Technol.* **50**, 1294–1305. https://doi.org/10.1080/02786826.2016.1221050 (2016).

26. Renbaum-Wolff, L., Grayson, J. W. & Bertram, A. K. Technical Note: New methodology for measuring viscosities in small volumes characteristic of environmental chamber particle samples. *Atmos. Chem. Phys.* **13**, 791–802. https://doi.org/10.5194/acp-13-791-2013 (2013).
27. Zhang, Y. *et al.* Changing shapes and implied viscosities of suspended submicron particles. *Atmos. Chem. Phys.* **15**, 7819–7829. https://doi.org/10.5194/acp-15-7819-2015 (2015).
28. Fitzgerald, C. *et al.* Fluorescence lifetime imaging of optically levitated aerosol: a technique to quantitatively map the viscosity of suspended aerosol particles. *Phys. Chem. Chem. Phys.* **18**, 21710–21719. https://doi.org/10.1039/C6CP03674K (2016).
29. Power, R. M., Simpson, S. H., Reid, J. P. & Hudson, A. J. The transition from liquid to solid-like behaviour in ultrahigh viscosity aerosol particles. *Chem. Sci.* **4**, 2597–2604. https://doi.org/10.1039/C3SC50682G (2013).
30. Renbaum-Wolff, L. *et al.* Viscosity of α-pinene secondary organic material and implications for particle growth and reactivity. *Proc. Natl. Acad. Sci.* **110**, 8014–8019. https://doi.org/10.1073/pnas.1219548110 (2013).
31. Koop, T., Bookhold, J., Shiraiwa, M. & Pöschl, U. Glass transition and phase state of organic compounds: dependency on molecular properties and implications for secondary organic aerosols in the atmosphere. *Phys. Chem. Chem. Phys.* **13**, 19238–19255. https://doi.org/10.1039/C1CP22617G (2011).
32. Shiraiwa, M. *et al.* Global distribution of particle phase state in atmospheric secondary organic aerosols. *Nat. Commun.* **8**, 15002 (2017).
33. Grayson, J. W. *et al.* The effect of hydroxyl functional groups and molar mass on the viscosity of non-crystalline organic and organic-water particles. *Atmos. Chem. Phys.* **17**, 8509–8524. https://doi.org/10.5194/acp-17-8509-2017 (2017).
34. Champion, W. M., Rothfuss, N. E., Petters, M. D. & Grieshop, A. P. Volatility and viscosity are correlated in Terpene secondary organic aerosol formed in a flow reactor. *Environ. Sci. Technol. Lett.* **6**, 513–519. https://doi.org/10.1021/acs.estlett.9b00412 (2019).
35. Zhang, Y. *et al.* The cooling rate- and volatility-dependent glass-forming properties of organic aerosols measured by broadband dielectric spectroscopy. *Environ. Sci. Technol.* https://doi.org/10.1021/acs.est.9b03317 (2019).
36. Bateman, A. P., Bertram, A. K. & Martin, S. T. Hygroscopic influence on the semisolid-to-liquid transition of secondary organic materials. *J. Phys. Chem. A* **119**, 4386–4395. https://doi.org/10.1021/jp508521c (2015).
37. Song, M. *et al.* Relative humidity-dependent viscosities of isoprene-derived secondary organic material and atmospheric implications for isoprene-dominant forests. *Atmos. Chem. Phys.* **15**, 5145–5159. https://doi.org/10.5194/acp-15-5145-2015 (2015).
38. Pajunoja, A. *et al.* Adsorptive uptake of water by semisolid secondary organic aerosols. *Geophys. Res. Lett.* **42**, 3063–3068. https://doi.org/10.1002/2015GL063142 (2015).
39. Saukko, E. *et al.* Humidity-dependent phase state of SOA particles from biogenic and anthropogenic precursors. *Atmos. Chem. Phys.* **12**, 7517–7529. https://doi.org/10.5194/acp-12-7517-2012 (2012).
40. Petters, S. S., Kreidenweis, S. M., Grieshop, A. P., Ziemann, P. J. & Petters, M. D. Temperature- and humidity-dependent phase states of secondary organic aerosols. *Geophys. Res. Lett.* **46**, 1005–1013. https://doi.org/10.1029/2018GL080563 (2019).
41. Slade, J. H. *et al.* Bouncier particles at night: biogenic secondary organic aerosol chemistry and sulfate drive diel variations in the aerosol phase in a mixed forest. *Environ. Sci. Technol.* **53**, 4977–4987. https://doi.org/10.1021/acs.est.8b07319 (2019).
42. Olson, N. E. *et al.* Reactive uptake of isoprene epoxydiols increases the viscosity of the core of phase-separated aerosol particles. *ACS Earth Space Chem.* **3**, 1402–1414. https://doi.org/10.1021/acsearthspacechem.9b00138 (2019).
43. Bell, D. M., Imre, D. T., Martin, S. & Zelenyuk, A. The properties and behavior of α-pinene secondary organic aerosol particles exposed to ammonia under dry conditions. *Phys. Chem. Chem. Phys.* **19**, 6497–6507. https://doi.org/10.1039/C6CP08839B (2017).
44. Rothfuss, N. E. & Petters, M. D. Characterization of the temperature and humidity-dependent phase diagram of amorphous nanoscale organic aerosols. *Phys. Chem. Chem. Phys.* **19**, 6532–6545. https://doi.org/10.1039/C6CP08593H (2017).
45. Marsh, A. *et al.* Amorphous phase state diagrams and viscosity of ternary aqueous organic/organic and inorganic/organic mixtures. *Phys. Chem. Chem. Phys.* **20**, 15086–15097. https://doi.org/10.1039/C8CP00760H (2018).
46. Järvinen, E. *et al.* Observation of viscosity transition in α-pinene secondary organic aerosol. *Atmos. Chem. Phys.* **16**, 4423–4438. https://doi.org/10.5194/acp-16-4423-2016 (2016).
47. Chenyakin, Y. *et al.* Diffusion coefficients of organic molecules in sucrose-water solutions and comparison with Stokes–Einstein predictions. *Atmos. Chem. Phys.* **17**, 2423–2435. https://doi.org/10.5194/acp-17-2423-2017 (2017).
48. Ullmann, D. A. *et al.* Viscosities, diffusion coefficients, and mixing times of intrinsic fluorescent organic molecules in brown limonene secondary organic aerosol and tests of the Stokes–Einstein equation. *Atmos. Chem. Phys.* **19**, 1491–1503. https://doi.org/10.5194/acp-19-1491-2019 (2019).
49. Maclean, A. M. *et al.* Mixing times of organic molecules within secondary organic aerosol particles: a global planetary boundary layer perspective. *Atmos. Chem. Phys.* **17**, 13037–13048. https://doi.org/10.5194/acp-17-13037-2017 (2017).
50. Tolman, R. C. Consideration of the Gibbs theory of surface tension. *J. Chem. Phys.* **16**, 758–774. https://doi.org/10.1063/1.1746994 (1948).
51. Samsonov, V., Sdobnyakov, N. & Bazulev, A. Size dependence of the surface tension and the problem of Gibbs thermodynamics extension to nanosystems. in *A Collection of Papers presented at XVIth European Chemistry at Interfaces Conference, 14–18 May, 2003, Vladimir, Russia* vol. 239, 113–117. https://doi.org/10.1016/j.colsurfa.2004.01.016 (2004).
52. Biskos, G., Malinowski, A., Russell, L. M., Buseck, P. R. & Martin, S. T. Nanosize effect on the deliquescence and the efflorescence of sodium chloride particles. *Aerosol Sci. Technol.* **40**, 97–106. https://doi.org/10.1080/02786820500484396 (2006).
53. Biskos, G., Paulsen, D., Russell, L. M., Buseck, P. R. & Martin, S. T. Prompt deliquescence and efflorescence of aerosol nanoparticles. *Atmos. Chem. Phys.* **6**, 4633–4642. https://doi.org/10.5194/acp-6-4633-2006 (2006).
54. Russell, L. M. & Ming, Y. Deliquescence of small particles. *J. Chem. Phys.* **116**, 311–321. https://doi.org/10.1063/1.1420727 (2001).
55. Biskos, G., Russell, L. M., Buseck, P. R. & Martin, S. T. Nanosize effect on the hygroscopic growth factor of aerosol particles. *Geophys. Res. Lett.* https://doi.org/10.1029/2005GL025199 (2006).
56. Levdanskii, V. V., Smolik, J. & Moravec, P. Influence of size effects on the critical diameter and growth of nanoparticles. *J. Eng. Phys. Thermophys.* **79**, 217–221. https://doi.org/10.1007/s10891-006-0089-y (2006).
57. Altaf, M. B., Zuend, A. & Freedman, M. A. Role of nucleation mechanism on the size dependent morphology of organic aerosol. *Chem. Commun.* **52**, 9220–9223. https://doi.org/10.1039/C6CC03826C (2016).
58. Veghte, D. P., Altaf, M. B. & Freedman, M. A. Size dependence of the structure of organic aerosol. *J. Am. Chem. Soc.* **135**, 16046–16049. https://doi.org/10.1021/ja408903g (2013).
59. Laskina, O. *et al.* Size matters in the water uptake and hygroscopic growth of atmospherically relevant multicomponent aerosol particles. *J. Phys. Chem. A* **119**, 4489–4497. https://doi.org/10.1021/jp510268p (2015).
60. Werner, J. *et al.* Surface partitioning in organic-inorganic mixtures contributes to the size-dependence of the phase-state of atmospheric nanoparticles. *Environ. Sci. Technol.* **50**, 7434–7442. https://doi.org/10.1021/acs.est.6b00789 (2016).
61. Virtanen, A. *et al.* Bounce behavior of freshly nucleated biogenic secondary organic aerosol particles. *Atmos. Chem. Phys.* **11**, 8759–8766. https://doi.org/10.5194/acp-11-8759-2011 (2011).
62. Cheng, Y., Su, H., Koop, T., Mikhailov, E. & Pöschl, U. Size dependence of phase transitions in aerosol nanoparticles. *Nat. Commun.* **6**, 5923 (2015).

63. Kaptay, G. The Gibbs equation versus the Kelvin and the Gibbs–Thomson equations to describe nucleation and equilibrium of nano-materials. *J. Nanosci. Nanotechnol.* **12**, 2625–2633. https://doi.org/10.1166/jnn.2012.5774 (2012).
64. Campbell, C. T., Parker, S. C. & Starr, D. E. The effect of size-dependent nanoparticle energetics on catalyst sintering. *Science* **298**, 811–814. https://doi.org/10.1126/science.1075094 (2002).
65. Letellier, P., Mayaffre, A. & Turmine, M. Melting point depression of nanosolids: nonextensive thermodynamics approach. *Phys. Rev. B* **76**, 045428. https://doi.org/10.1103/PhysRevB.76.045428 (2007).
66. Jiang, Q., Yang, C. C. & Li, J. C. Size-dependent melting temperature of polymers. *Macromol. Theory Simul.* **12**, 57–60. https://doi.org/10.1002/mats.200390003 (2003).
67. David, T. B., Lereah, Y., Deutscher, G., Kofman, R. & Cheyssac, P. Solid–liquid transition in ultra-fine lead particles. *Philos. Mag. A* **71**, 1135–1143. https://doi.org/10.1080/01418619508236241 (1995).
68. Wronski, C. R. M. The size dependence of the melting point of small particles of tin. *Br. J. Appl. Phys.* **18**, 1731–1737. https://doi.org/10.1088/0508-3443/18/12/308 (1967).
69. Castro, T., Reifenberger, R., Choi, E. & Andres, R. P. Size-dependent melting temperature of individual nanometer-sized metallic clusters. *Phys. Rev. B* **42**, 8548–8556. https://doi.org/10.1103/PhysRevB.42.8548 (1990).
70. Wunderlich, B. & Czornyj, G. A study of equilibrium melting of polyethylene. *Macromolecules* **10**, 906–913. https://doi.org/10.1021/ma60059a006 (1977).
71. Angell, C. A. Formation of glasses from liquids and biopolymers. *Science* **267**, 1924. https://doi.org/10.1126/science.267.5206.1924 (1995).
72. Angell, C. A. Liquid fragility and the glass transition in water and aqueous solutions. *Chem. Rev.* **102**, 2627–2650. https://doi.org/10.1021/cr000689q (2002).
73. Longinotti, M. P. & Corti, H. R. Viscosity of concentrated sucrose and trehalose aqueous solutions including the supercooled regime. *J. Phys. Chem. Ref. Data* **37**, 1503–1515. https://doi.org/10.1063/1.2932114 (2008).
74. Gordon, M. & Taylor, J. S. Ideal copolymers and the second-order transitions of synthetic rubbers. I. non-crystalline copolymers. *J. Appl. Chem.* **2**, 493–500. https://doi.org/10.1002/jctb.5010020901 (1952).
75. Baustian, K. J. *et al.* State transformations and ice nucleation in amorphous (semi-)solid organic aerosol. *Atmos. Chem. Phys.* **13**, 5615–5628. https://doi.org/10.5194/acp-13-5615-2013 (2013).
76. Wang, B. *et al.* The deposition ice nucleation and immersion freezing potential of amorphous secondary organic aerosol: pathways for ice and mixed-phase cloud formation. *J. Geophys. Res. Atmos.* https://doi.org/10.1029/2012JD018063 (2012).
77. Lienhard, D. M., Zobrist, B., Zuend, A., Krieger, U. K. & Peter, T. Experimental evidence for excess entropy discontinuities in glass-forming solutions. *J. Chem. Phys.* **136**, 074515. https://doi.org/10.1063/1.3685902 (2012).
78. Petters, M. D. & Kreidenweis, S. M. A single parameter representation of hygroscopic growth and cloud condensation nucleus activity—part 2: including solubility. *Atmos. Chem. Phys.* **8**, 6273–6279. https://doi.org/10.5194/acp-8-6273-2008 (2008).
79. Mikhailov, E., Vlasenko, S., Rose, D. & Pöschl, U. Mass-based hygroscopicity parameter interaction model and measurement of atmospheric aerosol water uptake. *Atmos. Chem. Phys.* **13**, 717–740. https://doi.org/10.5194/acp-13-717-2013 (2013).
80. Pinal, R. Entropy of mixing and the glass transition of amorphous mixtures. *Entropy.* https://doi.org/10.3390/entropy-e10030207 (2008).
81. Fox, T. G. Influence of diluent and of copolymer composition on the glass temperature of a polymer system. *Bull. Am. Phys. Soc.* **1**, 123 (1956).
82. Couchman, P. R. & Karasz, F. E. A classical thermodynamic discussion of the effect of composition on glass-transition temperatures. *Macromolecules* **11**, 117–119. https://doi.org/10.1021/ma60061a021 (1978).
83. Kwei, T. K. The effect of hydrogen bonding on the glass transition temperatures of polymer mixtures. *J. Polym. Sci. Polym. Lett. Ed.* **22**, 307–313. https://doi.org/10.1002/pol.1984.130220603 (1984).
84. Suda, S. R. *et al.* Hygroscopicity frequency distributions of secondary organic aerosols. *J. Geophys. Res. Atmos.* https://doi.org/10.1029/2011JD016823 (2012).
85. Heaton, K. J., Sleighter, R. L., Hatcher, P. G., Hall, W. A. & Johnston, M. V. Composition domains in monoterpene secondary organic aerosol. *Environ. Sci. Technol.* **43**, 7797–7802. https://doi.org/10.1021/es901214p (2009).
86. Drake, A. C. *et al.* Effect of water content on the glass transition temperature of mixtures of sugars, polymers, and penetrating cryoprotectants in physiological buffer. *PLOS ONE* **13**, e0190713. https://doi.org/10.1371/journal.pone.0190713 (2018).
87. DeRieux, W.-S.W. *et al.* Predicting the glass transition temperature and viscosity of secondary organic material using molecular composition. *Atmos. Chem. Phys.* **18**, 6331–6351. https://doi.org/10.5194/acp-18-6331-2018 (2018).
88. Abramson, E., Imre, D., Beránek, J., Wilson, J. & Zelenyuk, A. Experimental determination of chemical diffusion within secondary organic aerosol particles. *Phys. Chem. Chem. Phys.* **15**, 2983–2991. https://doi.org/10.1039/C2CP44013J (2013).
89. Kidd, C., Perraud, V., Wingen, L. M. & Finlayson-Pitts, B. J. Integrating phase and composition of secondary organic aerosol from the ozonolysis of α-pinene. *Proc. Natl Acad. Sci.* **111**, 7552–7557. https://doi.org/10.1073/pnas.1322558111 (2014).
90. Pajunoja, A. *et al.* Estimating the viscosity range of SOA particles based on their coalescence time. *Aerosol Sci. Technol.* **48**, i–iv. https://doi.org/10.1080/02786826.2013.870325 (2014).
91. Grayson, J. W. *et al.* Effect of varying experimental conditions on the viscosity of α-pinene derived secondary organic material. *Atmos. Chem. Phys.* **16**, 6027–6040. https://doi.org/10.5194/acp-16-6027-2016 (2016).
92. Bateman, A. P., Belassein, H. & Martin, S. T. Impactor apparatus for the study of particle rebound: relative humidity and capillary forces. *Aerosol Sci. Technol.* **48**, 42–52. https://doi.org/10.1080/02786826.2013.853866 (2014).
93. Li, Y., Day, D. A., Stark, H., Jimenez, J. & Shiraiwa, M. Predictions of the glass transition temperature and viscosity of organic aerosols by volatility distributions. *Atmos. Chem. Phys. Discuss.* https://doi.org/10.5194/acp-2019-1132 (2020).
94. Petters, M. D., Kreidenweis, S. M. & Ziemann, P. J. Prediction of cloud condensation nuclei activity for organic compounds using functional group contribution methods. *Geosci. Model Dev.* **9**, 111–124. https://doi.org/10.5194/gmd-9-111-2016 (2016).
95. Petters, M. D. *et al.* Role of molecular size in cloud droplet activation. *Geophys. Res. Lett.* https://doi.org/10.1029/2009GL040131 (2009).
96. Akbulut, S. *et al.* Solid–liquid interfacial energy of pyrene. *J. Appl. Phys.* **100**, 123505. https://doi.org/10.1063/1.2402098 (2006).
97. Wong, W.-K. & Westrum, E. F. Thermodynamics of polynuclear aromatic molecules I. Heat capacities and enthalpies of fusion of pyrene, fluoranthene, and triphenylene. *J. Chem. Thermodyn.* **3**, 105–124. https://doi.org/10.1016/S0021-9614(71)80071-X (1971).
98. Chen, D., Totton, T. S., Akroyd, J. W., Mosbach, S. & Kraft, M. Size-dependent melting of polycyclic aromatic hydrocarbon nano-clusters: a molecular dynamics study. *Carbon* **67**, 79–91. https://doi.org/10.1016/j.carbon.2013.09.058 (2014).
99. Koppes, J. P., Muza, A. R., Stach, E. A. & Handwerker, C. H. Comment on "Size-dependent melting properties of small tin particles: nanocalorimetric measurements". *Phys. Rev. Lett.* **104**, 189601. https://doi.org/10.1103/PhysRevLett.104.189601 (2010).
100. Lai, S. L., Guo, J. Y., Petrova, V., Ramanath, G. & Allen, L. H. Size-dependent melting properties of small tin particles: nanocalorimetric measurements. *Phys. Rev. Lett.* **77**, 99–102. https://doi.org/10.1103/PhysRevLett.77.99 (1996).
101. Lu, H. M., Li, P. Y., Cao, Z. H. & Meng, X. K. Size-, shape-, and dimensionality-dependent melting temperatures of nanocrystals. *J. Phys. Chem. C* **113**, 7598–7602. https://doi.org/10.1021/jp900314q (2009).
102. Dick, K., Dhanasekaran, T., Zhang, Z. & Meisel, D. Size-dependent melting of silica-encapsulated gold nanoparticles. *J. Am. Chem. Soc.* **124**, 2312–2317. https://doi.org/10.1021/ja017281a (2002).

103. Jackson, C. L. & McKenna, G. B. The melting behavior of organic materials confined in porous solids. *J. Chem. Phys.* **93**, 9002–9011. https://doi.org/10.1063/1.459240 (1990).
104. Rothe, M. & Rothe, I. Physical data of oligomers. In *Polymer Handbook* 3rd edn (eds Brandrup, J. & Immergut, E. H.) IV/2 (Wiley, New York, 1989).
105. Rothe, M. & Rothe, I. Physical data of oligomers. In *Polymer Handbook* 3rd edn (eds Brandrup, J. & Immergut, E. H.) IV/4 (Wiley, New York, 1989).
106. Petters, M. D. & Kreidenweis, S. M. A single parameter representation of hygroscopic growth and cloud condensation nucleus activity. *Atmos. Chem. Phys.* **7**, 1961–1971. https://doi.org/10.5194/acp-7-1961-2007 (2007).
107. Varutbangkul, V. *et al.* Hygroscopicity of secondary organic aerosols formed by oxidation of cycloalkenes, monoterpenes, sesquiterpenes, and related compounds. *Atmos. Chem. Phys.* **6**, 2367–2388. https://doi.org/10.5194/acp-6-2367-2006 (2006).
108. Petters, M. D. *et al.* Towards closing the gap between hygroscopic growth and activation for secondary organic aerosol—part 2: theoretical approaches. *Atmos. Chem. Phys.* **9**, 3999–4009. https://doi.org/10.5194/acp-9-3999-2009 (2009).
109. Kuwata, M., Zorn, S. R. & Martin, S. T. Using elemental ratios to predict the density of organic material composed of carbon, hydrogen, and oxygen. *Environ. Sci. Technol.* **46**, 787–794. https://doi.org/10.1021/es202525q (2012).
110. Pokluda, O., Bellehumeur, C. T. & Vlachopoulos, J. Modification of Frenkel's model for sintering. *AIChE J.* **43**, 3253–3256. https://doi.org/10.1002/aic.690431213 (1997).

Acknowledgements

Author contributions

M.D.P. wrote the main manuscript text. M.D.P. and S.K. collected and analyzed the data. All authors reviewed the manuscript.

Competing interests

The authors declare no competing interests.

Additional information

Supplementary information is available for this paper at https://doi.org/10.1038/s41598-020-71490-0.

Correspondence and requests for materials should be addressed to M.P.

Reprints and permissions information is available at www.nature.com/reprints.

Publisher's note Springer Nature remains neutral with regard to jurisdictional claims in published maps and institutional affiliations.